ACS APPLIED MATERIALS & INTERFACES

Research Article

Cite This: ACS Appl. Mater. Interfaces 2018, 10, 8909−8916

www.acsami.org

Electronic Level Alignment at an Indium Tin Oxide/PbI_2 Interface and Its Applications for Organic Electronic Devices

Qiaogang Song,[†,‡] Tong Lin,[†,‡] Xue Sun,[†,‡] Bei Chu,[†] Zisheng Su,*[,†,§] Huishan Yang,*[,§] Wenlian Li,[†] and Chun Sing Lee[∥]

[†]State Key Laboratory of Luminescence and Applications, Changchun Institute of Optics, Fine Mechanics and Physics, Chinese Academy of Sciences, Changchun 130033, P. R. China

[‡]University of Chinese Academy of Sciences, Beijing 100049, P. R. China

[§]College of Physics and Information Engineering, Quanzhou Normal University, Quanzhou 362000, P. R. China

[∥]Center of Super-Diamond and Advanced Films (COSDAF) and Department of Chemistry, City University of Hong Kong, Hong Kong 999077, P. R. China

Supporting Information

ABSTRACT: The electronic level alignment at the indium tin oxide (ITO)/PbI_2 interface is investigated by an ultraviolet photoelectron spectroscopy. An n-type conductivity property is found for PbI_2 as well as a downward shift energy level at the ITO/PbI_2 interface. These indicate that PbI_2 can be used as an anode buffer layer for organic electronic devices. The power conversion efficiency of the organic solar cell based on tetraphenyldibenzoperiflanthene/C_{70} planar heterojunction is dramatically increased from 1.05 to 3.82%. Meanwhile, the thermally activated delayed fluorescence organic light-emitting diode based on 4,4′,4″-tri(*N*-carbazolyl)triphenylamine−((1,3,5-triazine-2,4,6-triyl)tris(benzene-3,1-diyl))tris(diphenylphosphine oxide) shows a significantly reduced turn-on voltage and enhanced power efficiency from 6.26 to 18.60 lm/W. The improved performance is attributed to the high hole injection/extraction efficiency at the ITO/PbI_2 interface. Besides, the near-infrared (NIR) absorption of lead phthalocyanine (PbPc)-based NIR organic photodetector (NIR-OPD) is dramatically increased, indicating that the PbI_2 layer can also be used as a template layer for the growth of the triclinic phase of PbPc. As a result, the optimized device shows an external quantum efficiency of 26.7% and a detectivity of 9.96×10^{11} jones at 900 nm, which are among the highest ones reported for organic NIR-OPDs.

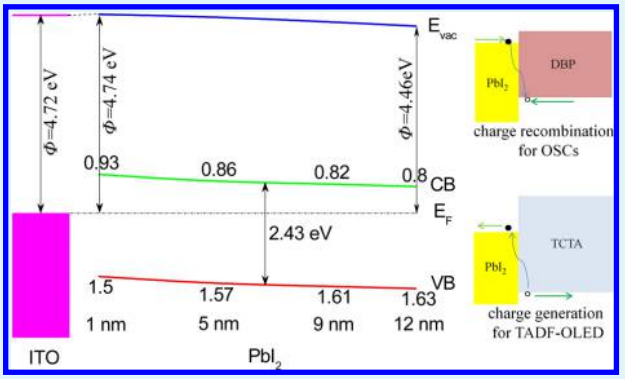

KEYWORDS: *lead iodide, n-type semiconductor, anode buffer layer, organic electronic devices*

1. INTRODUCTION

Since the reports of high-performance photovoltaic and electroluminescent devices based on organic compounds by Tang and VanSlyke,[1,2] organic electronic devices have attracted much attention because of their intrinsic potential of low cost, lightweight, flexible, large absorption coefficient, abundant, simple fabricated process, and large area. These devices include organic light-emitting diodes (OLEDs),[3−5] organic solar cells (OSCs),[6,7] organic photodetectors (OPDs),[8,9] and organic transistors.[10,11] The performance of these devices is highly dependent on their interface properties between different layers, such as organic/organic and metal/organic interfaces.[12,13] Interface engineering is one of the efficient technologies to tune the interface properties and hence the performance of the devices.[14] The interface between the anode and organic layer has drawn more and more attention. In the past few years, significant efforts have been devoted to the research of the electronic level at indium tin oxide (ITO)/organic interfaces and their applications as anode buffer layers. The commonly used anode buffer layers are p-type organic or inorganic materials with suitable energy level and conductivity to insure a high hole injection or extraction efficiency, such as poly(3,4-ethylenedioxythiophene):poly(styrenesulfonate) (PEDOT:PSS),[15,16] copper(II) phthalocyanine,[17] CuI,[18,19] and NiO_x.[20,21] The hole injection or extraction is through their valance band maximum (VBM) or highest occupied molecular orbital (HOMO) levels. More interestingly, n-type transition-metal oxides can also be adopted as the anode buffer layer, such as MoO_x,[22−24] V_2O_x,[22,23] and WO_x.[25,26] Correspondingly, a different mechanism is proposed, where the hole injection is through the electron transfer from the HOMO of the hole-transporting layer (HTL) to the conduction band minimum (CBM) of the anode buffer layer, whereas the hole extraction is via the electron injection from their CBM and then recombines

Received: December 20, 2017
Accepted: February 21, 2018
Published: February 21, 2018

DOI: 10.1021/acsami.7b19376
ACS Appl. Mater. Interfaces 2018, 10, 8909−8916

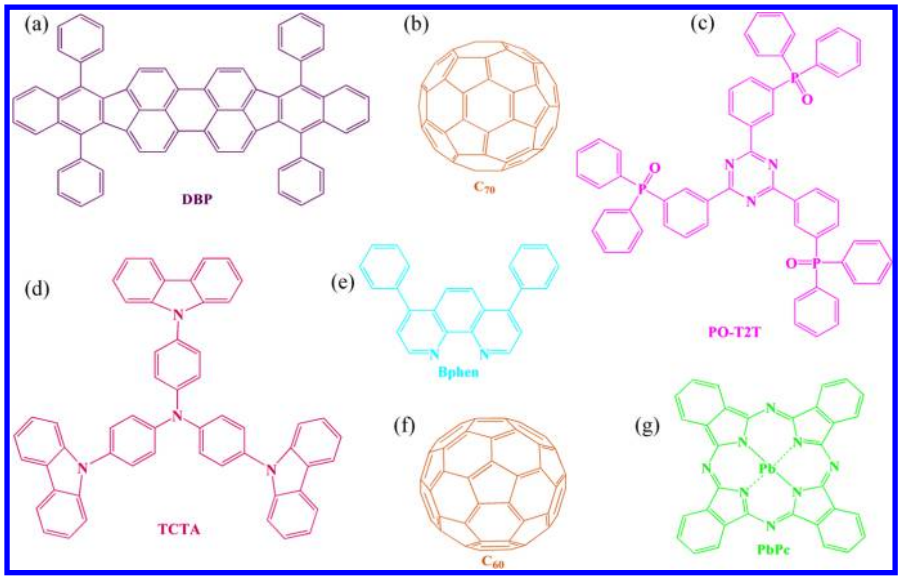

Figure 1. Organic molecular structures of (a) DBP, (b) C_{70}, (c)PO-T2T, (d) TCTA, (e) Bphen, (f) C_{60}, and (g) PbPc.

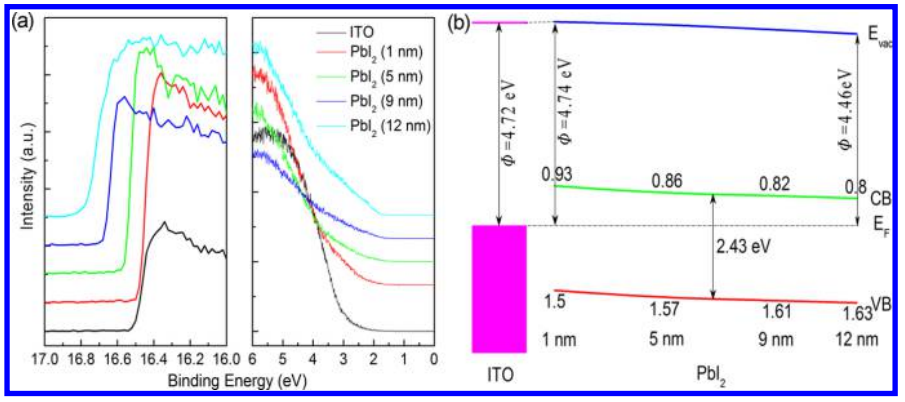

Figure 2. (a) UPS spectra of PbI_2 on top of ITO with different thicknesses. (b) Energy level diagram at the ITO/PbI_2 interface.

with a hole in the HTL. As a result, their hole-transporting property highly relies on their CBM which depends on their stoichiometric composition and will change in different environments.[27] Besides, these transition-metal oxides usually have a high evaporation temperature.

Lead iodide (PbI_2) is a semiconductor with a band gap of about 2.43 eV and has been widely used as the active material for X-ray and γ-ray detectors.[28,29] Recently, it has been used as one of the precursors of the tremendous perovskite solar cells.[30−32] Here, the electronic level alignment at the ITO/PbI_2 interface is investigated by an ultraviolet photoelectron spectroscopy (UPS). An n-type conductivity is found for PbI_2 as well as a downward shift energy level at the ITO/PbI_2 interface. On the basis of the energy level alignment at the ITO/PbI_2 interface, PbI_2 is adopted as an anode buffer for OSCs, OLEDs, and OPDs. The power conversion efficiency (PCE) of the OSC based on tetraphenyldibenzoperiflanthene (DBP)/C_{70} planar heterojunction is dramatically increased from 1.05 to 3.82% after the insertion of PbI_2, which is comparable and even a little higher than that with a traditional MoO_3 (3.58%) or CuI (3.50%) buffer layer. On the other hand, the thermally activated delayed fluorescence (TADF)-OLED based on 4,4′,4″-tri(*N*-carbazolyl)triphenylamine (TCTA)−((1,3,5-triazine-2,4,6-triyl)tris(benzene-3,1-diyl))tris-(diphenylphosphine oxide) (PO-T2T) shows a significantly reduced turn-on voltage and enhanced power efficiency from 6.26 to 18.60 lm/W. The improvements are attributed to the increased hole extraction/injection efficiency of the devices. Moreover, PbI_2 can be used not only as a buffer layer but also as a template for the growth of the triclinic phase of lead phthalocyanine (PbPc), which increases the near-infrared (NIR) absorption of the PbPc-based OPDs and hence the response of the devices. These results indicate that PbI_2 can be used as an efficient anode buffer layer for organic electronic devices.

2. EXPERIMENTAL SECTION

All materials are commercially available without further purification, and their molecular structures are shown in Figure 1. All of the films and devices were fabricated on ITO-coated glass substrates with a thickness of about 140 nm and a sheet resistance of 15 Ω/sq. The substrates were cleaned by ultrasonication in sequence in acetone, deionized water, and isopropanol for 10 min and dried naturally. Then, they were treated in an ultraviolet−ozone chamber for 15 min before loading into a vacuum chamber. All layers were thermally evaporated in the vacuum chamber with a pressure of 5×10^{-4} Pa. The electronic levels were measured with a UPS (VG Scienta R3000) at a pressure of about 5×10^{-8} Pa. The structure of the OSCs used here is ITO/PbI_2/DBP (20 nm)/C_{70} (50 nm)/4,7-diphenyl-1,10-phenanthroline (Bphen, 8 nm)/Al (100 nm). For reference, devices with a traditional MoO_3 or CuI buffer layer were also fabricated. The TADF-OLEDs have the structure of ITO/PbI_2/TCTA (31 nm)/TCTA−PO-T2T

DOI: 10.1021/acsami.7b19376
ACS Appl. Mater. Interfaces 2018, 10, 8909−8916

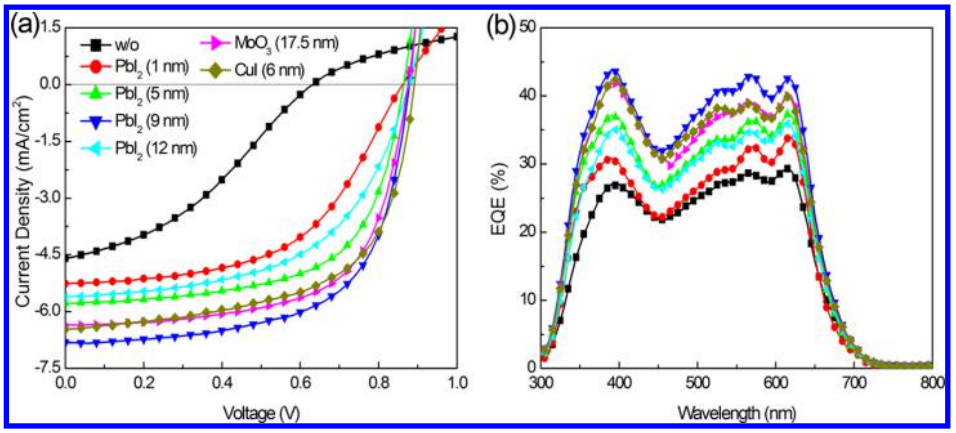

Figure 3. (a) $J-V$ characteristic and (b) IPCE spectra of the OSCs ITO/anode buffer layer/DBP (20 nm)/C_{70} (50 nm)/Bphen (8 nm)/Al (100 nm) with PbI_2, MoO_3, and CuI anode buffer layers.

(1:1, 31 nm)/PO-T2T (60 nm)/LiF (1.5 nm)/Al (100 nm). The NIR-OPDs have a structure of ITO/PbI_2/PbPc (75 nm)/C_{60} (80 nm)/Al (100 nm). The thickness and deposition rates were monitored by quartz crystal sensors. The MoO_3, PbI_2, and CuI were deposited at a rate of 0.5 Å/s, organic materials were deposited at a rate of 1 Å/s, LiF was deposited at a rate of 0.25 Å/s, and Al was deposited at a rate of 10 Å/s. The area of all of the devices was 2.5 × 4 mm^2. The current–voltage ($J-V$) characteristics of OSCs and NIR-OPDs were measured with a source meter (Keithley 2400) in dark and under illumination of an AM 1.5G solar simulator (Newport 94023A). The incident photon-to-current conversion efficiency (IPCE) spectra were obtained with a lock-in amplifier (Stanford SR830) under monochromatic illumination at a chopping frequency of 130 Hz by a chopper (Stanford SR540). Luminance–current–voltage characteristics of the TADF-OLEDs were measured by using a source meter (Keithley 2400) with a luminance meter (Minolta LS-160). Steady-state electroluminescence (EL) spectra were measured with an OPT-2000 spectrophotometer. Absorption spectra were measured with a UV–vis–NIR spectrophotometer (Shimadzu, UV-3101PC). X-ray diffraction (XRD) patterns were measured with a diffractometer (Rigaku D/Max 2500) using Cu Kα radiation (λ = 1.54056 Å). All measurements were characterized in an ambient environment without encapsulation.

3. RESULTS AND DISCUSSION

3.1. Electronic Level Alignment at the ITO/PbI_2 Interface. The energy level alignment at the ITO/PbI_2 interface with different thicknesses of PbI_2 is investigated with UPS, as shown in Figure 2a. The secondary electron cutoff position of pristine ITO locates at 16.50 eV, indicating that it has a work function of 4.72 eV, whereas the secondary electron cutoff position of 1 nm PbI_2 locates at 16.48 eV, corresponding to a Fermi level of 4.74 eV. This indicates a small upward shift of the vacuum level of 0.02 eV at the ITO/PbI_2 interface. The onset of VBM of 1 nm PbI_2 is 1.5 eV. In view of a band gap of 2.43 eV deduced from the absorption spectrum PbI_2, the CBM is 0.93 eV higher than its Fermi level. Gradually increasing the thickness of PbI_2 to 12 nm leads to a shift of the secondary electron cutoff position toward higher binding energy, which equivalents to a decrease of the work function and a downward shift of the vacuum level. As a result, the work function of 12 nm PbI_2 is 4.46 eV. On the other hand, the onset of VBM is increased to 1.63 eV, indicating a larger distance between the VBM and Fermi energy level and vice versa for the distance between the CBM and Fermi energy level, as shown in the energy level alignment in Figure 2b. More interestingly, the Fermi level of PbI_2 is near to the CBM especially at higher thickness, suggesting the intrinsic n-type conductivity of PbI_2. The n-type conductivity of PbI_2 has also been demonstrated recently by Hu et al. with a thin PbI_2 layer thermally evaporated on the SnO_x layer.[33]

3.2. PbI_2 as an Anode Buffer Layer for OSCs. Similar to other reported n-type materials, PbI_2 may also be used as the anode buffer layer for organic electronic devices. We first examine this role in a small molecular solar cell. The $J-V$ curves of the DBP/C_{70} planar heterojunction OSCs with various thicknesses of PbI_2 under illumination of an AM 1.5G solar simulator with an intensity of 100 mW/cm^2 are shown in Figure 3a. Detail photovoltaic parameters of the devices extracted from the curves are summarized in Table 1. The

Table 1. Device Performance of the OSCs ITO/Anode Buffer Layer/DBP (20 nm)/C_{70} (50 nm)/Bphen (8 nm)/Al (100 nm) with Different Anode Buffer Layers

buffer layer	thickness (nm)	V_{on} (V)	J_{sc} (mA/cm^2)	FF	PCE (%)
PbI_2	0	0.63	4.60	0.36	1.05
	1	0.86	5.26	0.53	2.42
	5	0.86	5.79	0.62	3.12
	9	0.88	6.82	0.64	3.82
	12	0.88	5.60	0.55	2.71
MoO_3	17.5	0.89	6.36	0.63	3.58
CuI	6	0.89	6.46	0.61	3.50

device without an anode buffer layer has a typical S-shape $J-V$ curve, indicating a large series resistance (R_s) and charge carrier recombination of the device. As a result, the PCE is only 1.05%, corresponding to an open-circuit voltage (V_{oc}) of 0.63 V, a short-circuit current (J_{sc}) of 4.60 mA/cm^2, and a fill factor (FF) of 0.36. The S-shape $J-V$ curve is entirely eliminated with the introduction of a PbI_2 anode buffer layer. The V_{oc}, J_{sc}, and especially FF are dramatically improved. The optimized device with a PbI_2 thickness of 9 nm shows a V_{oc} of 0.88 V, a J_{sc} of 6.82 mA/cm^2, and a FF of 0.64, corresponding to a PCE of 3.82%, which is 3.6 times to the reference device without an anode buffer layer. Further increase of the thickness of PbI_2 up to 12 nm, the PCE markedly decreases to 2.71%. Figure 3b displays the IPCE spectra of the devices. All of the devices exhibit a broad response in the visible region from 350 to 650 nm. Moreover, the IPCE of the devices with a PbI_2 anode buffer layer is higher than that of the reference device without PbI_2 in

DOI: 10.1021/acsami.7b19376
ACS Appl. Mater. Interfaces 2018, 10, 8909–8916

the whole response region, which is consistent with the J_{sc} found in their $J-V$ curves.

MoO_3[34−36] and CuI[37] have widely been used as the anode buffer layers for OSCs. To compare the effect of the anode buffer layer on the performance of the OSC, DBP/C_{70} heterojunction-based OSCs with a MoO_3 or CuI anode buffer layer were also fabricated. The $J-V$ curves of these devices are shown in Figures S1 and S2, and the detail photovoltaic parameters are summarized in Tables S1 and S2. The device with an optimized MoO_3 buffer layer (17.5 nm) shows a V_{oc} of 0.89 V, a J_{sc} of 6.36 mA/cm^2, and a FF of 0.63, corresponding to a PCE of 3.58%, whereas the device with an optimized CuI buffer layer (6 nm) shows a V_{oc} of 0.89 V, a J_{sc} of 6.46 mA/cm^2, and a FF of 0.61, corresponding to a PCE of 3.50%, as shown in Figure 3a. This suggests that the PCE of the device with a PbI_2 anode buffer layer is comparable and even a little higher than that based on either a MoO_3 or CuI buffer layer.

For an OSC, the PCE is typically determined by four factors, as follows

$$\mathrm{PCE} = \eta_{\mathrm{Abs}} \times \eta_{\mathrm{ED}} \times \eta_{\mathrm{CG}} \times \eta_{\mathrm{CC}} \quad (1)$$

where η_{Abs} is the light absorption efficiency, η_{ED} is the exciton diffusion efficiency at the donor−acceptor (D−A) interface, η_{CG} is the charge generation efficiency at the D−A interface, and η_{CC} is the carrier collection efficiency by the electrodes. Because of the similar D−A interface, η_{ED} and η_{CG} are assumed to be the same for all of the devices. Figure 4 draws the

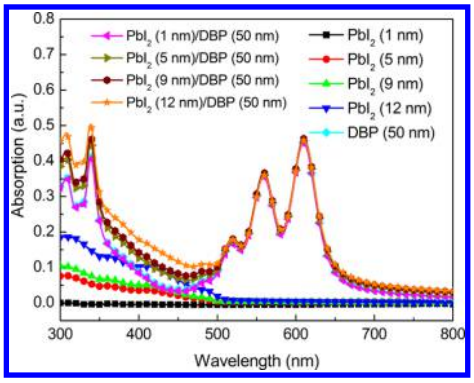

Figure 4. Absorption spectra of PbI_2, DBP, and DBP films on PbI_2.

absorption spectra of PbI_2, DBP, and DBP films on PbI_2. PbI_2 layers primary absorb in the region with a wavelength shorter than 510 nm, corresponding to a band gap of about 2.43 eV. DBP has a broad absorption band at 500 to 650 nm. Interestingly, the absorption band of DBP films on PbI_2 presents the same shape and intensity, indicating that the introduction of a PbI_2 anode buffer layer has no effect on the absorption of DBP films. On the other hand, the increased absorption with the PbI_2 layer thickness at a wavelength shorter than 500 nm is attributed to the increased absorption of PbI_2. These findings rule out the absorption contributed to the improved performance of the OSCs. Thus, the only possible mechanism is the increased charge carrier collection efficiency, and in this situation, it should be the hole collection efficiency.

In an OSC, the major origin of the S-shape $J-V$ curve has been reported to result from the imbalanced carrier mobility, accumulated charge carrier, interface barrier, and undesirable dipole formation.[38] The HOMO level of DBP is 5.5 eV,[39] suggesting that there is a high energy barrier of 0.78 eV for hole extraction from DBP to ITO. This results in an S-shape $J-V$ curve of the device, as shown in Figure 3. The VBM and CBM of 9 nm PbI_2 are 6.33 and 3.90 eV, respectively. Thus, holes cannot be extracted directly from the VBM of PbI_2. Meyer et al.[40] reported that a charge recombination layer is formed in the n-type MoO_3/DBP interface, and the photogenerated holes in DBP can drift to this interface and recombine with electrons injected from the CBM of MoO_3 and finally accomplish the hole extraction process. Similar to this mechanism, holes in our devices can also be extracted with such an electron−hole recombination process at the PbI_2/DBP interface. Meanwhile, such a recombination process is more efficient than direct transport of holes from DBP to ITO in extracting the photogenerated holes. As a result, the J_{sc} of the devices is dramatically improved (Figure 3). The improved hole collection efficiency also reduces the electron−hole recombination in the bulk of the active layer, which increases the V_{oc} and decreases the R_s of the devices simultaneously.

The stability is another key parameter for OSCs. To test the stability of the OSCs with different anode buffer layers, the devices were continuous exposed to an AM 1.5G solar simulator with an intensity of 100 mW/cm^2. The decreases of the normalized PCE with illumination time are shown in Figure S3. The device without any anode buffer layer exhibits a most serious degradation, whereas the devices with PbI_2 and CuI show the highest stability, which is even a little higher than that with a MoO_3 anode buffer layer. These results indicate that PbI_2 can be used as an efficient and stable anode buffer layer of OSCs.

3.3. PbI_2 as an Anode Buffer Layer for OLEDs. In OSCs, PbI_2 is used as a buffer layer to extract photogenerated holes. To elucidate its hole injection property for other organic electronic devices, PbI_2 is further used as an anode buffer layer for OLEDs. Recently, TADF-OLEDs which rely on the reverse intersystem crossing via thermal activation have attracted great attention because of their low cost, simple structure, and the same internal quantum efficiency of 100% in theory to that of phosphorescent OLEDs.[4,5] Hung et al.[41] have demonstrated an efficient exciplex emission from a TCTA−PO-T2T bilayer system with TADF properties. In their devices, a PEDOT:PSS/*N*,*N*′-bis-(1-naphthyl)-*N*,*N*′-diphenyl-1,1′-biphenyl-4,4′-diamine (NPB) bilayer structure was used as the anode buffer layer. In this work, TADF-OLEDs with a TCTA−PO-T2T mixed emitting layer were constructed. The EL spectra of the devices are displayed in Figure S4. All of the devices show an EL peak at about 557 nm, which is similar to the report by Hung et al.[41] The characteristics of the devices are shown in Figure 5, and the detailed performance is summarized in Table 2. The device without PbI_2 shows a high turn-on voltage of 5.3 V; consequently, the device has a power efficiency of 6.26 lm/W. In contrast, the insertion of a PbI_2 anode buffer layer dramatically reduces the turn-on voltage to about 2.4 V and increases the current density of the devices. As a result, the power efficiency is significantly boosted. The optimized device with 5 nm PbI_2 exhibits a maximum power efficiency of 18.60 lm/W, which is three times to the reference device without PbI_2. Besides, this device also has a maximum luminance of 25353 cd/m^2 and a maximum external quantum efficiency (EQE) of 6.42%. These parameters are comparable to the reported device with a PEDOT:PSS/NPB anode buffer layer, suggesting that this bilayer anode buffer layer can be displayed by PbI_2 to simplify the device structure. On the other hand, compared with the power efficiency, a moderate increased EQE

DOI: 10.1021/acsami.7b19376
ACS Appl. Mater. Interfaces 2018, 10, 8909−8916

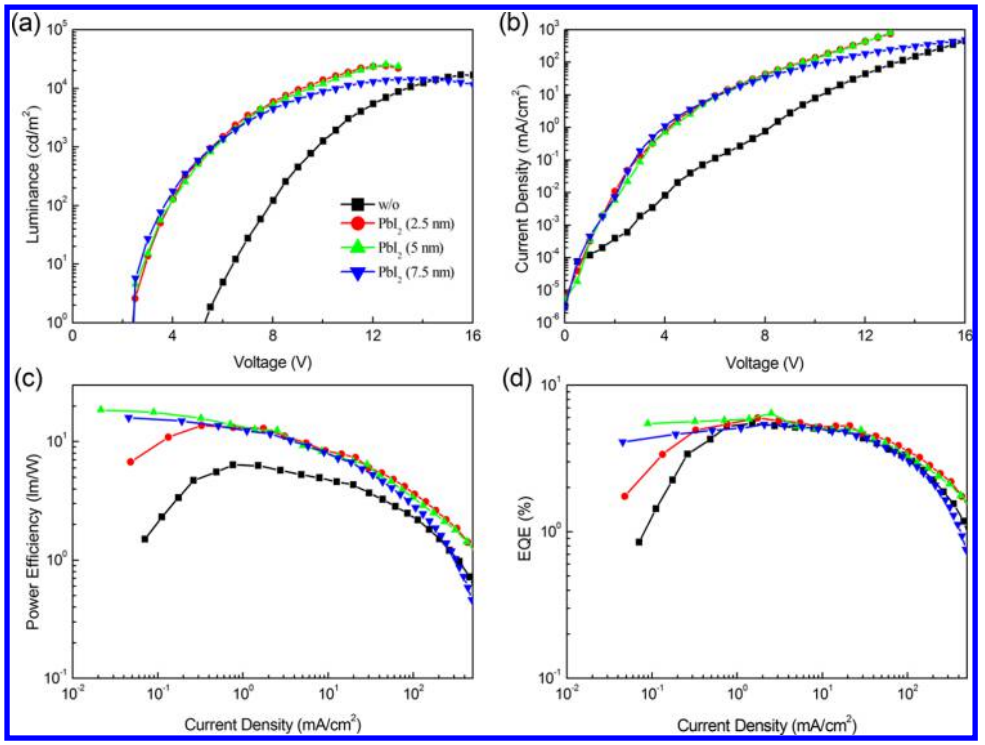

Figure 5. (a) Luminance−voltage characteristics, (b) voltage−current density characteristics, (c) current density−power efficiency characteristics, and (d) current density−EQE characteristics of the OLEDs with different buffer layers.

Table 2. Device Performance of the TADF-OLEDs with Different Buffer Layers[a]

PbI_2 thickness (nm)	V_{on} (V)	L_{max} (cd/m²)	η_P (lm/W)	EQE (%)
0	5.3	16799@15.5 V	6.26	5.48
2.5	2.4	24245@12.5 V	13.69	5.98
5	2.4	25353@12.5 V	18.60	6.42
7.5	2.3	14313@13.5 V	15.93	5.41

[a] V_{on}: turn-on voltage, L_{max}: maximum luminance, and η_P: power efficiency.

of about 17% is observed, which should be attributed to the dramatically increased current density of the device.

The HOMO energy level of TCTA is 5.7 eV,[42] which indicates that there is a 0.98 eV energy barrier for holes injection from ITO. This large energy barrier results in a high turn-on voltage of the device without an anode buffer layer. Similarly, the VBM of 5 nm PbI_2 is 6.22 eV (Figure 2), and the holes cannot be direct injected from ITO to TCTA via the VBM of PbI_2. In terms of the n-type property of PbI_2, electrons in the HOMO of TCTA will inject to the CBM of PbI_2 and then recombination with holes in ITO, leaving a large number of holes in the HOMO of TCTA, and finally inject to the emitting layer.[24]

3.4. PbI_2 as an Anode Buffer Layer for OPDs. A NIR-OPD is a type of organic electronic device other than OSC and OLED and has large potential applications in national defense and society. However, because of the lack of narrow band gap organic materials, rare NIR-OPDs have been reported.[43−45] PbPc is a shuttlecock-shape molecule with a high absorption coefficient in the NIR region which originates from the triclinic phase of PbPc in the film. To increase the triclinic phase formation, a template layer, such as CuI[46−48] and pentacene,[49] is often used to control the growth of the PbPc film. As discussed in the front, PbI_2 can be used as an efficient anode buffer layer for OSCs to extract photogenerated holes. Here, PbI_2 is used as an anode buffer layer as well as a template layer for a PbPc-based NIR-OPD.

Figure 6 shows the absorption spectra of the PbPc films on CuI and PbI_2 template layers. The pristine PbPc film has a NIR

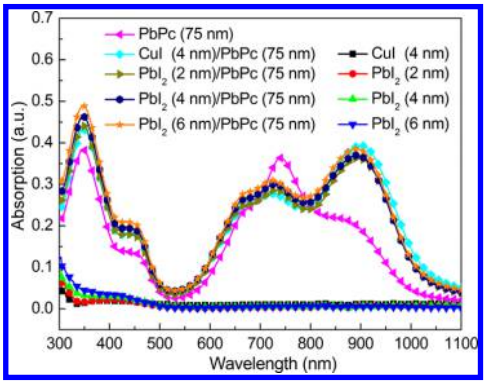

Figure 6. Absorption spectra of the films on quartz substrates.

absorption band at about 740 nm with a shoulder at about 900 nm, which are attributed to the absorptions of the monoclinic and triclinic phases, respectively. After inserting a thin PbI_2 layer, the absorption of the triclinic phase is dramatically increased, which is similar to that on the CuI template layer. This suggests that PbI_2 can really be used as a template for the growth of the triclinic phase of PbPc, which can be further confirmed by the XRD patterns of PbPc shown in Figure S5. The diffraction peak at 2θ of 12.6° which can be attributed to the $(11\bar{1})$ reflection plane of the triclinic phase of PbPc is increased after the insertion of PbI_2, indicating that the PbI_2

DOI: 10.1021/acsami.7b19376
ACS Appl. Mater. Interfaces 2018, 10, 8909−8916

buffer layer leads to the preferred growth of the triclinic phase of PbPc in the films.

The dark currents of the NIR-OPDs with different anode buffer layers are displayed in Figure S6. It can be found that the currents of the devices with PbI_2 layers at the positive region are increased compared with the device without any buffer layer, which is consistence with the result found in OLEDs, suggesting that the hole injection is improved by the insertion of the PbI_2 layer. In contrast, the dark currents in the negative region of these devices are comparable. It can also find that the device with a CuI layer has the lowest current in the negative region. This should be attributed to the higher CBM of CuI, which blocks the injection of electrons. Figure 7 shows the

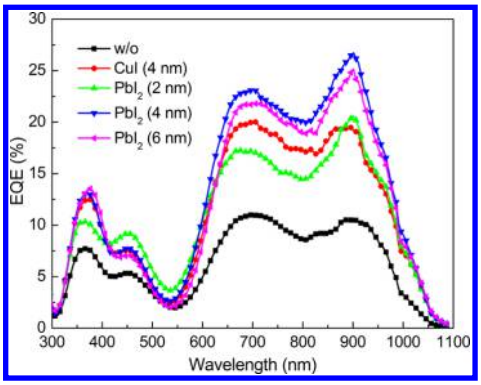

Figure 7. EQE spectra at zero bias of the OPDs ITO/anode buffer layer/PbPc (75 nm)/C_{60} (80 nm)/Al (100 nm) with different anode buffer layers.

EQE spectra of the devices at zero bias. These devices exhibit a broadband response that covers the wavelengths range from 300 to 1100 nm with the maximum response at the NIR region. The maximum EQE of the device without PbI_2 is 10.5% at 900 nm, whereas it is 19.6% for the device with a CuI layer. The EQE of the devices is dramatically increased by the insertion of PbI_2. The optimized device with a 4 nm PbI_2 layer shows a maximum EQE of 26.7% at 900 nm, which is about 2.5 times to the device without a buffer layer and 1.4 times to the device with a CuI layer. The detectivity (D^*) is another important parameter for a photodetector. Under zero bias, the D^* can be calculated with the equation[50]

$$D^* = R \cdot \sqrt{A \cdot R_D / 4k_B T} \quad (2)$$

where R is the responsivity, A is the area, R_D is the zero-bias differential resistance of the device, k_B is the Boltzmann constant, and T is the temperature. The calculated D^* of the devices is shown in Figure S7. The D^* of the optimized device is on the order of 10^{10} jones in the whole response range, and in particular, it reaches to 10^{11} jones in the NIR region. The maximum D^* of the optimized device is 9.96×10^{11} jones at 900 nm, which is six times to the reference device without PbI_2 buffer layers. The D^* is also higher than the one with a CuI layer, which is attributed to its higher EQE. Such a D^* is one of the highest ones reported for small-molecular NIR-OPDs.[43−45] The improvement is attributed to the increased EQE of the device, which contributed to the simultaneously increased absorption and hole collection efficiency.

As demonstrated above, the performance of the NIR-OPDs can be improved with either a PbI_2 or CuI anode buffer layer. Because PbI_2 and CuI have the common point of containing iodide, it is necessary to clarify the effects of the iodide on the film growth of PbPc. We further use $PbCl_2$ and $PbBr_2$ as the anode buffer layers for the NIR-OPDs. The EQE spectra of these devices are shown in Figure S8. However, no improvement is obtained in these devices. The difference should be attributed to their difference in the halogen, which may result in different energy levels, conductivities, and surface properties. This indicates that the growth of triclinic phase PbPc may result from the iodide. Further work is required to gain more insight about the mechanism.

4. CONCLUSIONS

In summary, the electronic level at the ITO/PbI_2 interface is illuminated by UPS, and an n-type conductivity is found for PbI_2. On the basis of this finding, PbI_2 is used as the anode buffer layer for OSCs, OLEDs, and NIR-OPDs. The performance of all of these devices is dramatically improved, which can be attributed to the high hole injection/extraction efficiency at the ITO/PbI_2 interface. Besides, PbI_2 can be used as the template for the triclinic phase growth of the PbPc film, making a more pronounce increase of the response. These results suggest that PbI_2 can be used as an efficient anode buffer layer for organic electronic devices.

■ ASSOCIATED CONTENT

Supporting Information

The Supporting Information is available free of charge on the ACS Publications website at DOI: 10.1021/acsami.7b19376.

J−*V* characteristic of OSCs with different thicknesses of MoO_3 and CuI, stability of OSCs with different anode buffer layers, normalized EL spectra of TCTA−PO-T2T-based TADF-OLEDs, XRD pattern of PbPc films, dark current of the NIR-OPDs, D^* of the NIR-OPDs, and EQE spectra of OPDs with $PbCl_2$ and $PbBr_2$ anode buffer layers (PDF)

■ AUTHOR INFORMATION

Corresponding Authors

*E-mail: suzs@ciomp.ac.cn (Z.S.).
*E-mail: yanghuishan1697@163.com (H.Y.).

ORCID

Zisheng Su: 0000-0001-6514-3596
Chun Sing Lee: 0000-0001-6557-453X

Notes

The authors declare no competing financial interest.

■ ACKNOWLEDGMENTS

This work was supported by the National Natural Science Foundation of China grants 61575192, 61376062, and 61376022.

■ REFERENCES

(1) Tang, C. W. Two-Layer Organic Photovoltaic Cell. *Appl. Phys. Lett.* **1986**, *48*, 183−185.
(2) Tang, C. W.; VanSlyke, S. A. Organic Electroluminescent Diodes. *Appl. Phys. Lett.* **1987**, *51*, 913−915.
(3) Forrest, S. R.; Baldo, M. A.; O'Brien, D. F.; You, Y.; Shoustikov, A.; Sibley, S.; Thompson, M. E. Highly Efficient Phosphorescent Emission from Organic Electroluminescent Devices. *Nature* **1998**, *395*, 151−154.
(4) Goushi, K.; Yoshida, K.; Sato, K.; Adachi, C. Organic Light-Emitting Diodes Employing Efficient Reverse Intersystem Crossing for Triplet-to-Singlet State Conversion. *Nat. Photonics* **2012**, *6*, 253−258.

DOI: 10.1021/acsami.7b19376
ACS Appl. Mater. Interfaces 2018, 10, 8909−8916

(5) Uoyama, H.; Goushi, K.; Shizu, K.; Nomura, H.; Adachi, C. Highly Efficient Organic Light-Emitting Diodes from Delayed Fluorescence. *Nature* **2012**, *492*, 234−238.
(6) He, Z.; Xiao, B.; Liu, F.; Wu, H.; Yang, Y.; Xiao, S.; Wang, C.; Russell, T. P.; Cao, Y. Single-Junction Polymer Solar Cells with High Efficiency and Photovoltage. *Nat. Photonics* **2015**, *9*, 174−179.
(7) Xiao, Z.; Jia, X.; Li, D.; Wang, S.; Geng, X.; Liu, F.; Chen, J.; Yang, S.; Russell, T. P.; Ding, L. 26 mA cm^{-2} J_{SC} from Organic Solar Cells with a Low-Bandgap Nonfullerene Acceptor. *Sci. Bull.* **2017**, *62*, 1494−1496.
(8) Gong, X.; Tong, M.; Xia, Y.; Cai, W.; Moon, J. S.; Cao, Y.; Yu, G.; Shieh, C.-L.; Nilsson, B.; Heeger, A. J. High-Detectivity Polymer Photodetectors with Spectral Response from 300 nm to 1450 nm. *Science* **2009**, *325*, 1665−1667.
(9) Wang, W.; Zhang, F.; Du, M.; Li, L.; Zhang, M.; Wang, K.; Wang, Y.; Hu, B.; Fang, Y.; Huang, J. Highly Narrowband Photomultiplication Type Organic Photodetectors. *Nano Lett.* **2017**, *17*, 1995−2002.
(10) Dodabalapur, A.; Katz, H. E.; Torsi, L.; Haddon, R. C. Organic Heterostructure Field-Effect Transistors. *Science* **1995**, *269*, 1560−1562.
(11) Nikolka, M.; Nasrallah, I.; Rose, B.; Ravva, M. K.; Broch, K.; Sadhanala, A.; Harkin, D.; Charmet, J.; Hurhangee, M.; Brown, A.; Illig, S.; Too, P.; Jongman, J.; McCulloch, I.; Bredas, J.-L.; Sirringhaus, H. High Operational and Environmental Stability of High-Mobility Conjugated Polymer Field-Effect Transistors through the Use of Molecular Additives. *Nat. Mater.* **2017**, *16*, 356−362.
(12) Ishii, H.; Sugiyama, K.; Ito, E.; Seki, K. Energy Level Alignment and Interfacial Electronic Structures at Organic/Metal and Organic/Organic Interfaces. *Adv. Mater.* **1999**, *11*, 605−625.
(13) Braun, S.; Salaneck, W. R.; Fahlman, M. Energy-Level Alignment at Organic/Metal and Organic/Organic Interfaces. *Adv. Mater.* **2009**, *21*, 1450−1472.
(14) Ma, H.; Yip, H.-L.; Huang, F.; Jen, A. K.-Y. Interface Engineering for Organic Electronics. *Adv. Funct. Mater.* **2010**, *20*, 1371−1388.
(15) de Jong, M. P.; van Ijzendoorn, L. J.; de Voigt, M. J. A. Stability of the Interface Between Indium-Tin-Oxide and Poly(3,4-ethylenedioxythiophene)/Poly(styrenesulfonate) in Polymer Light-Emitting Diodes. *Appl. Phys. Lett.* **2000**, *77*, 2255−2257.
(16) Zhou, T.; Xie, G.; Gong, S.; Huang, M.; Luo, J.; Yang, C. Simple $InCl_3$ Doped PEDOT:PSS and UV−Ozone Treatment Strategy: External Quantum Efficiency up to 21% for Solution-Processed Organic Light-Emitting Devices with a Thermally Activated Delayed Fluorescence Emitter. *ACS Appl. Mater. Interfaces* **2017**, *9*, 34139−34145.
(17) Ke, W.; Zhao, D.; Grice, C. R.; Cimaroli, A. J.; Fang, G.; Yan, Y. Efficient Fully-Vacuum-Processed Perovskite Solar Cells Using Copper Phthalocyanine as Hole Selective Layers. *J. Mater. Chem. A* **2015**, *3*, 23888−23894.
(18) Peng, Y.; Yaacobi-Gross, N.; Perumal, A. K.; Faber, H. A.; Vourlias, G.; Patsalas, P. A.; Bradley, D. D. C.; He, Z.; Anthopoulos, T. D. Efficient Organic Solar Cells Using Copper(I) Iodide (CuI) Hole Transport Layers. *Appl. Phys. Lett.* **2015**, *106*, 243302.
(19) Christians, J. A.; Fung, R. C. M.; Kamat, P. V. An Inorganic Hole Conductor for Organo-Lead Halide Perovskite Solar Cells. Improved Hole Conductivity with Copper Iodide. *J. Am. Chem. Soc.* **2014**, *136*, 758−764.
(20) Bao, Z.-M.; Xu, R.-P.; Li, C.; Xie, Z.-Z.; Zhao, X.-D.; Zhang, Y.-B.; Li, Y.-Q.; Tang, J.-X. Switching Hole and Electron Transports of Molecules on Metal Oxides by Energy Level Alignment Tuning. *ACS Appl. Mater. Interfaces* **2016**, *8*, 22410−22417.
(21) Li, Y.-H.; Lu, X.; Wang, R.; Ma, Y.-Y.; Duhm, S.; Fung, M.-K. Cu-Doped Nickel Oxide Prepared Using a Low-Temperature Combustion Method as a Hole-Injection Layer for High-Performance OLEDs. *J. Mater. Chem. C* **2017**, *5*, 11751−11757.
(22) Shrotriya, V.; Li, G.; Yao, Y.; Chu, C.-W.; Yang, Y. Transition Metal Oxides as the Buffer Layer for Polymer Photovoltaic Cells. *Appl. Phys. Lett.* **2006**, *88*, 073508.
(23) Li, X.; Xie, F.; Zhang, S.; Hou, J.; Choy, W. C. H. MoO_x and V_2O_x as Hole and Electron Transport Layers through Functionalized Intercalation in Normal and Inverted Organic Optoelectronic Devices. *Light: Sci. Appl.* **2015**, *4*, e273.
(24) Kröger, M.; Hamwi, S.; Meyer, J.; Riedl, T.; Kowalsky, W.; Kahn, A. Role of the Deep-Lying Electronic States of MoO_3 in the Enhancement of Hole-Injection in Organic Thin Films. *Appl. Phys. Lett.* **2009**, *95*, 123301.
(25) Meyer, J.; Winkler, T.; Hamwi, S.; Schmale, S.; Johannes, H.-H.; Weimann, T.; Hinze, P.; Kowalsky, W.; Riedl, T. Transparent Inverted Organic Light-Emitting Diodes with a Tungsten Oxide Buffer Layer. *Adv. Mater.* **2008**, *20*, 3839−3843.
(26) Qiu, M.; Zhu, D.; Bao, X.; Wang, J.; Wang, X.; Yang, R. WO_3 with Surface Oxygen Vacancies as an Anode Buffer Layer for High Performance Polymer Solar Cells. *J. Mater. Chem. A* **2016**, *4*, 894−900.
(27) Irfan; Ding, H.; Gao, Y.; Small, G.; Kim, D. Y.; Subbiah, J.; So, F. Energy Level Evolution of Air and Oxygen Exposed Molybdenum Trioxide Films. *Appl. Phys. Lett.* **2010**, *96*, 243307.
(28) Fornaro, L.; Saucedo, E.; Mussio, L.; Gancharov, A.; Guimaraes, F.; Hernandes, A. Lead Iodide Platelets: Correlation Between Surface, Optical, and Electrical Properties With X- and γ-Ray Spectrometric Performance. *IEEE Trans. Nucl. Sci.* **2002**, *49*, 3300−3305.
(29) Matuchova, M.; Zdansky, K.; Zavadil, J.; Tonn, J.; Jafar, M. M. A.-G.; Danilewsky, A. N.; Cröll, A.; Maixner, J. Influence of Doping and Non-Stoichiometry on the Quality of Lead Iodide for Use in X-Ray Detection. *J. Cryst. Growth* **2010**, *312*, 1233−1239.
(30) Kojima, A.; Teshima, K.; Shirai, Y.; Miyasaka, T. Organometal Halide Perovskites as Visible-Light Sensitizers for Photovoltaic Cells. *J. Am. Chem. Soc.* **2009**, *131*, 6050−6051.
(31) Stranks, S. D.; Eperon, G. E.; Grancini, G.; Menelaou, C.; Alcocer, M. J.; Leijtens, T.; Herz, L. M.; Petrozza, A.; Snaith, H. J. Electron-Hole Diffusion Lengths Exceeding 1 Micrometer in an Organometal Trihalide Perovskite Absorber. *Science* **2013**, *342*, 341−344.
(32) Yang, W. S.; Park, B.-W.; Jung, E. H.; Jeon, N. J.; Kim, Y. C.; Lee, D. U.; Shin, S. S.; Seo, J.; Kim, E. K.; Noh, J. H.; Seok, S. I. Iodide Management in Formamidinium-Lead-Halide-Based Perovskite Layers for Efficient Solar Cells. *Science* **2017**, *356*, 1376−1379.
(33) Hu, T.; Becher, T.; Pourdavoud, N.; Zhao, J.; Brinkmann, K. O.; Heiderhoff, R.; Gahlmann, T.; Huang, Z.; Olthof, S.; Meerholz, K.; Többens, D.; Cheng, B.; Chen, Y.; Riedl, T. Indium-Free Perovskite Solar Cells Enabled by Impermeable Tin-Oxide Electron Extraction Layers. *Adv. Mater.* **2017**, *29*, 1606656.
(34) Girotto, C.; Voroshazi, E.; Cheyns, D.; Heremans, P.; Rand, B. P. Solution-Processed MoO_3 Thin Films as a Hole-Injection Layer for Organic Solar Cells. *ACS Appl. Mater. Interfaces* **2011**, *3*, 3244−3247.
(35) Su, Z.; Wang, L.; Li, Y.; Zhang, G.; Zhao, H.; Yang, H.; Ma, Y.; Chu, B.; Li, W. Surface Plasmon Enhanced Organic Solar Cells with a MoO_3 Buffer Layer. *ACS Appl. Mater. Interfaces* **2013**, *5*, 12847−12853.
(36) Kinoshita, Y.; Takenaka, R.; Murata, H. Independent Control of Open-Circuit Voltage of Organic Solar Cells by Changing Film Thickness of MoO_3 Buffer Layer. *Appl. Phys. Lett.* **2008**, *92*, 243309.
(37) Peng, Y.; Yaacobi-Cross, N.; Perumal, A. K.; Faber, H. A.; Vourlias, G.; Patsalas, P. A.; Bradley, D. D. C.; He, Z.; Anthopoulos, T. D. Efficient Organic Solar Cells using Copper(I) Iodide (CuI) Hole Transport Layers. *Appl. Phys. Lett.* **2015**, *106*, 243302.
(38) Lu, S.; Guan, X.; Li, X.; Liu, J.; Huang, F.; Choy, W. C. H. The Incorporation of Thermionic Emission and Work Function Tuning Layer into Intermediate Connecting Layer for High Performance Tandem Organic Solar Cells. *Nano Energy* **2016**, *21*, 123−132.
(39) Wang, Z.; Yokoyama, D.; Wang, X.-F.; Hong, Z.; Yang, Y.; Kido, J. Highly Efficient Organic p−i−n Photovoltaic Cells Based on Tetraphenyldibenzoperiflanthene and Fullerene C_{70}. *Energy Environ. Sci.* **2013**, *6*, 249−255.
(40) Meyer, J.; Hamwi, S.; Kröger, M.; Kowalsky, W.; Riedl, T.; Kahn, A. Transition Metal Oxides for Organic Electronics: Energetics, Device Physics and Applications. *Adv. Mater.* **2012**, *24*, 5408−5427.

DOI: 10.1021/acsami.7b19376
ACS Appl. Mater. Interfaces 2018, 10, 8909−8916

(41) Hung, W.-Y.; Fang, G.-C.; Lin, S.-W.; Cheng, S.-H.; Wong, K.-T.; Kuo, T.-Y.; Chou, P.-T. The First Tandem, All-exciplex-based WOLED. *Sci. Rep.* **2014**, *4*, 5161.
(42) Wu, Z.; Sun, N.; Zhu, L.; Sun, H.; Wang, J.; Yang, D.; Qiao, X.; Chen, J.; Alshehri, S. M.; Ahamad, T.; Ma, D. Achieving Extreme Utilization of Excitons by an Efficient Sandwich-Type Emissive Layer Architecture for Reduced Efficiency Roll-Off and Improved Operational Stability in Organic Light-Emitting Diodes. *ACS Appl. Mater. Interfaces* **2016**, *8*, 3150−3159.
(43) Hendriks, K. H.; Li, W.; Wienk, M. M.; Janssen, R. A. J. Small-Bandgap Semiconducting Polymers with High Near-Infrared Photoresponse. *J. Am. Chem. Soc.* **2014**, *136*, 12130−12136.
(44) Peng, W.; Liu, Y.; Wang, C.; Hu, R.; Zhang, J.; Xu, D.; Wang, Y. A Highly Sensitive Near-Infrared Organic Photodetector Based on Oxotitanium Phthalocyanine Nanocrystals and Light-Induced Enhancement of Electron Tunnelling. *J. Mater. Chem. C* **2015**, *3*, 5073−5077.
(45) Xiong, S.; Tong, J.; Mao, L.; Li, Z.; Qin, F.; Jiang, F.; Meng, W.; Liu, T.; Li, W.; Zhou, Y. Double-Side Responsive Polymer Near-Infrared Photodetectors with Transfer-Printed Electrode. *J. Mater. Chem. C* **2016**, *4*, 1414−1419.
(46) Kim, H. J.; Shim, H.-S.; Kim, J. W.; Lee, H. H.; Kim, J.-J. CuI Interlayers in Lead Phthalocyanine Thin Films Enhance Near-Infrared Light Absorption. *Appl. Phys. Lett.* **2012**, *100*, 263303.
(47) Wang, X.; Li, H.; Su, Z.; Fang, F.; Zhang, G.; Wang, J.; Chu, B.; Fang, X.; Wei, Z.; Li, B.; Li, W. Efficient Organic Near-Infrared Photodetectors Based on Lead Phthalocyanine/C_{60} Heterojunction. *Org. Electron.* **2014**, *15*, 2367−2371.
(48) Su, Z.; Hou, F.; Wang, X.; Gao, Y.; Jin, F.; Zhang, G.; Li, Y.; Zhang, L.; Chu, B.; Li, W. High-Performance Organic Small-Molecule Panchromatic Photodetectors. *ACS Appl. Mater. Interfaces* **2015**, *7*, 2529−2534.
(49) Zhao, W.; Mudrick, J. P.; Zheng, Y.; Hammond, W. T.; Yang, Y.; Xue, J. Enhancing Photovoltaic Response of Organic Solar Cells Using a Crystalline Molecular Template. *Org. Electron.* **2012**, *13*, 129−135.
(50) Arnold, M. S.; Zimmerman, J. D.; Renshaw, C. K.; Xu, X.; Lunt, R. R.; Austin, C. M.; Forrest, S. R. Broad Spectral Response Using Carbon Nanotube/Organic Semiconductor/C_{60} Photodetectors. *Nano Lett.* **2009**, *9*, 3354−3358.

DOI: 10.1021/acsami.7b19376
ACS Appl. Mater. Interfaces 2018, 10, 8909−8916